

# Pitting Mechanism of Mild Steel in Marginally Sour Environments: Pit Propagation Based on Acidification by Catalytic Oxidation of Dissolved Hydrogen Sulfide

Wei Zhang,<sup>‡,\*</sup> Bruce Brown,<sup>\*\*</sup> David Young,<sup>\*\*</sup> Stephen Smith,<sup>\*\*</sup> Sytze Huizinga,<sup>\*\*</sup> and Marc Singer<sup>\*\*</sup>

*The present work studies pit propagation in marginally sour environments and proposes a credible mechanism. Both thermodynamic calculation and experimental measurement confirmed that H<sub>2</sub>S can be oxidized by traces of dissolved O<sub>2</sub> into SO<sub>4</sub><sup>2-</sup> and H<sup>+</sup> in the aqueous solutions near room temperature with the transitional metal ions serving as a catalyst. This acidification phenomenon would be more effective near the steel surface, especially inside a pit, where Fe<sup>2+</sup> ions are most abundant. Therefore, the saturation degree of mackinawite would be lower inside the pit, which would prohibit the pitting from annihilation.*

KEY WORDS: carbon steel, hydrogen sulfide, oxygen, pitting, thermodynamics

## INTRODUCTION

Sour corrosion refers to reactions between H<sub>2</sub>S contained in natural gas or crude oil and steel used in petroleum environments. Different types of iron sulfide polymorphs formed on the steel surface under different H<sub>2</sub>S concentrations and temperatures, which lead to various damage to the steel. Therefore, there are subgroups under the term "sour corrosion" based on H<sub>2</sub>S concentration. Specifically, opposite to the high H<sub>2</sub>S concentration, there is one common type of field condition called "marginally sour" or "slightly sour".<sup>1</sup> It usually refers to a part per million (ppm) level of H<sub>2</sub>S concentration in the gas phase saturated with the crude and formation water (or production fluid). However, due to the difference in the total pressure, this definition is not rigorous enough.<sup>2</sup> Recently, some researchers argue that the definition should be based on the calculated saturation degree of FeS (mackinawite) from the dissolved H<sub>2</sub>S.<sup>3</sup> Marginally sour corrosion is a heated debated field due to the facts that: (1) this type of condition is common in many oil fields and (2) localized corrosion occurs more frequently under these conditions.<sup>2</sup>

A common characteristic of marginally sour environments is that they feature low partial pressure H<sub>2</sub>S that often translates into a saturation degree of FeS lower than unity. In other words, unless the surface pH and/or Fe<sup>2+</sup> concentration are high, no corrosion product is expected to precipitate in these conditions according to thermodynamic calculations. However, pitting was found in marginally sour environments repeatedly,<sup>1,3,4</sup> which should imply the presence of a partially protective layer or film on the substrate surface. A systematic parametric study indeed found that the occurrence of this type of pitting failure was related to the lack of protectiveness

of a mackinawite corrosion product layer, which could have formed through a chemisorption process.<sup>3</sup> It also found that the pH of the aqueous solution played a key role.<sup>3,5</sup> Analysis of the main constituents of the corrosion product layer identified the presence of sulfides but also of oxides, which was rather unexpected. Additional experiments were designed to trace the origin of these oxides and revealed that a minuscule degree of oxygen ingress during the completion of the tests was the reason why pitting occurred in marginally sour environments.<sup>5</sup> When the O<sub>2(aq)</sub> concentration was kept below 3 ppb<sub>(w)</sub>, the chemisorbed FeS layer [S<sub>ads</sub>(Fe)] was able to protect the steel surface from acidic corrosion caused by the presence of H<sup>+</sup>. However, this chemisorbed FeS layer could be oxidized by amounts of dissolved oxygen higher than 3 ppb<sub>(w)</sub>. Therefore, this partially oxidized layer was heterogeneous in terms of protectiveness. It was hypothesized that the volume change caused by the phase change led to exposure of the unprotected steel surface to the corrosive aqueous environment (H<sup>+</sup> and H<sub>2</sub>CO<sub>3(aq)</sub>). This mechanism was proposed to explain pit initiation in marginally sour environments.

This finding<sup>5</sup> has been widely accepted by corrosion engineers in oil production and service companies. It is also verified by two basic facts that: (1) oxygen levels in service are rarely measured by operators and (2) there have been failures in service attributed to poor control of oxygen levels. In the field, fresh water was used for chemical injection, and deoxygenation treatment is seldom used for most companies. As a routine, only CO<sub>2</sub> and H<sub>2</sub>S in the gas phase were sampled as required by operators, while O<sub>2</sub> concentration has never been included. The authors hope this finding would initiate the change in sour corrosion management by monitoring oxygen concentration.

Submitted for publication: April 20, 2021. Revised and accepted: December 1, 2021. Preprint available online: December 1, 2021, <https://doi.org/10.5006/3858>.

<sup>‡</sup> Corresponding author. E-mail: [wz521414@ohio.edu](mailto:wz521414@ohio.edu).

\* Schlumberger, 6350 W Sam Houston Pkwy N, Houston, Texas 77041.

\*\* Institute for Corrosion and Multiphase Technology, Ohio University, 342 West State Street, Athens, Ohio 45701.

However, back to the mechanism of sour pitting, two additional questions remained unanswered:

- (1) How do pits propagate in marginally sour environments?
- (2) Why does the pH decrease during the corrosion process when  $[O_2]_{aq} < 3 \text{ ppb}_{(w)}$ ?

Both thermodynamic calculations and experimental verifications are described in this work to address these two problems, which seem inevitably linked.

Traditional models of pit propagation often feature "a cathode of large area and an anode of small area." This means that while most of the area of the steel surface is protected, and acts as a cathode, small localized areas of the steel surface act anodically and experience environments conducive to sustained high corrosion rates. More specifically, to maintain a high corrosion rate inside the pit, the potential at the bottom of the pit must be lower than the surrounding area, or/and the water chemistry inside the pit must prevent the formation of a corrosion product layer. Usually, the latter scenario can be narrowed down to situations where the pH inside the pit is lower than in the bulk solution, or where some other aggressive ions ( $Cl^-$  in the case of stainless steel, for example) are present. Another factor to consider in localized corrosion is the conductivity of the corrosion product layer. If the layer has a larger electrical conductivity, the galvanic coupling effect between the actively corroding small area and the large protected area can be enhanced. Therefore, most of the pit propagation models couple mass transfer, electrochemical reactions, chemical reactions, potential and current density distributions inside of the pit, seeking depassivation, pit acidification, and galvanic coupling to support a higher corrosion rate in the pit.

In atmospheric corrosion, many metals experience passivation. Due to the stability of the passive layer, a stable pit growth could establish with a potential build inside the pit.<sup>6-8</sup> In aerated environments, at medium pH range (>4.5), hydrolysis of  $Fe^{3+}$  could produce  $H^+$  and thereby lead to pit acidification.<sup>9-10</sup> This lower pH would make the environment inside the pit more corrosive. The presence of "aggressive ions" such as  $Cl^-$  or  $SO_4^{2-}$  could also prevent repassivation.<sup>11</sup>

In  $CO_2$  corrosion environments, the "gray zone" theory has been used to explain both pit initiation and pit propagation.<sup>12</sup> When the saturation degree of  $FeCO_3$  inside the pit is less than unity, no  $FeCO_3$  layer can precipitate, thereby promoting pit propagation. Basically,  $[CO_3^{2-}]$  used in the saturation degree calculation is calculated from multiple dissolution steps from  $[H_2CO_3]$ , which is a function of temperature and  $CO_2$  partial pressure. Han<sup>13</sup> measured the galvanic coupling effect and surface pH value inside a pit and calculated the current density and potential distribution.<sup>14</sup> However, inside the pit, the pH naturally tends to increase due to the release of  $Fe^{2+}$  and consumption of  $H^+$ , increasing the saturation degree and making the environment paradoxically less corrosive and favorable for corrosion product precipitation. Only periodic changes in the environment or specific fluid flow conditions (top-of-the-line corrosion [TLC]<sup>15</sup> or high local turbulence level) can explain how saturation degree could remain less than unity.<sup>14</sup>

In  $H_2S/CO_2$  corrosion environments, the galvanic coupling effect occurring between the steel surface and pyrite<sup>16</sup> or pyrrhotite<sup>17</sup> was studied extensively. The existence of galvanic coupling in the presence of mackinawite remains to be identified due to its instability. However, the fact that the conductivity of mackinawite (metallic) is larger than pyrite (semiconducting)<sup>18</sup> and that the corrosion rate inside the pit was much higher than the mackinawite layer-free corrosion rate<sup>3</sup> seem to suggest that galvanic coupling does work when

mackinawite is the protective layer. Analysis of the bulk solution chemistry related to pitting in sour environments showed that  $H_2S$  can be oxidized into elemental sulfur,  $SO_3^{2-}$ , and  $SO_4^{2-}$ ,<sup>19</sup> but no effort was done to generate a potential current distribution between the pit and the surrounding area.

Because the occurrence of pitting in marginally sour environments can be directly linked to the presence of trace amounts of  $O_{2(aq)}$ ,<sup>5</sup> it is essential to investigate the effects of oxygen in detail.<sup>5</sup> Overall, the effect of the presence of dissolved oxygen on a sour corrosion system can be divided into three aspects: (1) oxygen can be directly reduced on the steel surface, adding an additional cathode reaction; (2) oxygen can react with  $H_2S$  in the aqueous solution producing multiple possible sulfur compounds as possible oxidation products; and (3) oxygen can induce the transformation of the corrosion product layer from ferrous sulfides (mackinawite) to ferric oxides (hematite).

The addition of the oxygen reduction reaction increases the general corrosion rate, but the added rate would be proportional to the dissolved  $O_2$  concentration, which is very small in this case, and may not be sufficient to explain the occurrence of pitting.<sup>5</sup> This will be discussed in more detail in this work.

Oxidation kinetics between  $H_2S$  and  $O_2$  has been studied extensively and typically leads to the formation of sulfite ( $SO_3^{2-}$ ), sulfate ( $SO_4^{2-}$ ), thiosulfate ( $S_2O_3^{2-}$ ), polysulfides ( $S_x^{2-}$ ), and elemental sulfur ( $S_8$ ).<sup>19-21</sup> When it happens in the gas phase, most often the application is in the synthesis of elemental sulfur or sulfuric acid. The most common industrial process for this is the well-described Claus process.  $V_2O_5$  was chosen as the catalyst in the sulfuric acid synthesis industry because it is the only transitional metal that can remain as an oxide rather than sulfide at a very high temperature (above  $250^\circ C$ ). The gas-phase  $H_2S$  oxidation reaction is reported not to occur below  $120^\circ C$ .<sup>22</sup> Oxidation of  $H_2S$  has also been reported to occur in the aqueous phase at lower (near room) temperatures, in the presence of dissolved oxygen. Two very common industrial applications use this reaction: oxygen scavengers<sup>23</sup> or water treatment.<sup>24</sup> Most published works naturally focus on the selection of highly efficient catalysts and on kinetic studies. Thermodynamic aspects have not experienced the same level of research focus and are as of yet not fully understood. The catalytic efficiency of transition metal oxides other than  $V_2O_5$ , such as Fe-, Ni-, Co-, and Cu-containing oxides (or salts of these metals), have been determined at low temperature in an aqueous solution.<sup>25</sup> However, in this case, the type of sulfur compounds produced depends on conditions such as temperature and reactant concentrations through the laws of thermodynamics, not the type of catalyst, which is a kinetic parameter. For instance, Dalai and co-workers reported that they could not experimentally identify elemental sulfur as a desired commercial byproduct of these oxidation reactions.<sup>24</sup> This is partly because there were no thermodynamic predictions in their research work. Therefore, thermodynamics of low-temperature, low-concentration  $H_2S$  oxidation will be revisited in this work. Water sample analysis and pH monitoring performed during the corrosion experiments are used to experimentally verify the thermodynamic predictions.

The crystallization process of mackinawite, its transformation and oxidation, are common topics of interest for geochemists.<sup>27</sup> Mackinawite can be formed homogeneously in freshwater environments. It can also precipitate heterogeneously, in the form of nanocrystals, and can easily be mistakenly reported as amorphous  $FeS$  by x-ray diffraction (XRD)<sup>25</sup> or electron diffraction. While the oxidation of mackinawite has been reported to occur in the absence of  $O_2$  above  $70^\circ C$  through

direct reaction with water,<sup>25</sup> most studies agree that oxygen is necessary, especially at a low temperature.<sup>26</sup> The most common products of mackinawite oxidation are greigite<sup>25</sup> and pyrite.<sup>27</sup> Greigite has been reported to form only at low pH, the reason being that the mackinawite crystal structure must first partially dissolve before transforming to form the greigite lattice.<sup>25</sup> Other products of mackinawite transformation could be goethite, magnetite, and hematite, depending on the presence of an aqueous phase and on temperature.<sup>27</sup> Thermodynamic calculation of oxidation of mackinawite will be discussed in this work together with the oxidation of dissolved H<sub>2</sub>S because both are related to the sulfur chemistry in sour corrosion.

**CONTRIBUTION OF THE O<sub>2</sub> REDUCTION TO THE OVERALL CATHODIC REACTION**

As stated in the introduction, the most straightforward effect brought by oxygen to an electrochemical system is its cathodic reduction. The presence of O<sub>2</sub> increases the general corrosion rate as its reduction can be added to the total cathodic reaction. However, given the small amount of O<sub>2</sub> ingress, this contribution is indeed minimal. As shown in Figure 1, calculated by a corrosion model (FRECORP<sup>28</sup>), the contribution of the O<sub>2</sub> reduction reaction to the total cathodic current density is negligible, even considering 1,000 ppb<sub>(w)</sub> of dissolved O<sub>2</sub>.

**THERMODYNAMICS OF THE OXIDATION OF DISSOLVED H<sub>2</sub>S AT LOW TEMPERATURES**

Multiple possible oxidation products of H<sub>2</sub>S have been reported, and are listed in Reactions (1) through (4); the calculated standard Gibbs free energies for these reactions are also listed. Most of the reactions release H<sup>+</sup> as a byproduct, except for Reaction (2). This means that the solution will tend to acidify only if the oxidation product of H<sub>2</sub>S is not elemental sulfur. The Pourbaix diagram and phase equilibrium diagrams are developed to determine which product is the most stable species at a given set of conditions (i.e., temperature, concentrations).

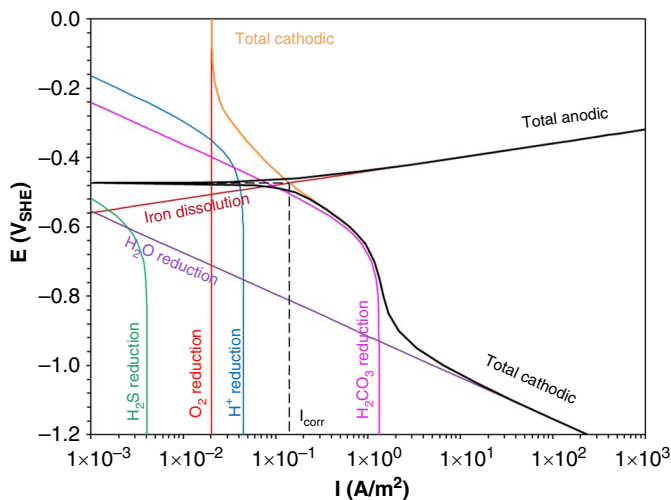
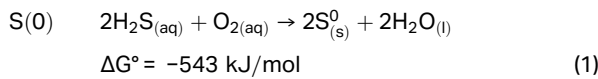
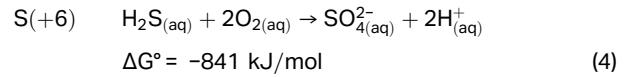
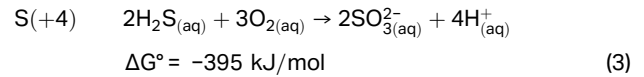
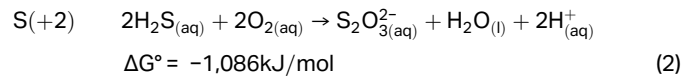
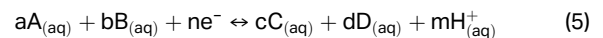


**FIGURE 1.** Evans diagram in marginally sour environment with O<sub>2</sub> (30°C, pH 5, 0.97 bar CO<sub>2</sub>, 0.04 mbar H<sub>2</sub>S, [O<sub>2</sub>]<sub>(aq)</sub> = 1 ppm<sub>(w)</sub>). Only the limiting current of the O<sub>2</sub> reduction is shown here.



Stability diagrams, such as Pourbaix diagrams, are frequently used to demonstrate the most stable species in an electrochemical system.<sup>29</sup> Usually, the x axis shows the most influential factor in water chemistry speciation—pH, while the y axis shows the equilibrium potential with respect to the standard hydrogen electrode (SHE) as calculated by the Nernst equation. The open-circuit potential (OCP) measured during the electrochemical experiments is the resting potential measured between working electrode and the environment (with respect to the reference electrode). The OCP is the potential at which the electrochemical system has reached a steady state, which is typically used as the potential of the electrochemical system in the Pourbaix diagram.<sup>30-31</sup> The Pourbaix diagram can be used to identify zones corresponding to the most thermodynamically stable species under a given pH and OCP. A Pourbaix diagram can be drawn based on electrochemical reactions written in a generalized form as in Reaction (5) and Equation (6).



$$E_H = E^\circ - \frac{RT}{nF} \left( \ln \frac{[C]^c [D]^d}{[A]^a [B]^b} - 2.303 \text{ mpH} \right) \quad (6)$$

As shown in Figure 2, a Pourbaix diagram of an aqueous solution saturated with p<sub>H<sub>2</sub>S</sub> = 1,000 Pa (0.01 bar) at 298.15 K was made to predict the oxidation product of H<sub>2</sub>S at the electrode surface. The thermodynamic data used is derived from the literature and handbook.<sup>32-34</sup> Equations related to the thermodynamic equilibrium are valid only taking into account the solution and the gases as ideals. Here, the transformation reactions used are listed in Equations (7) through (12). These

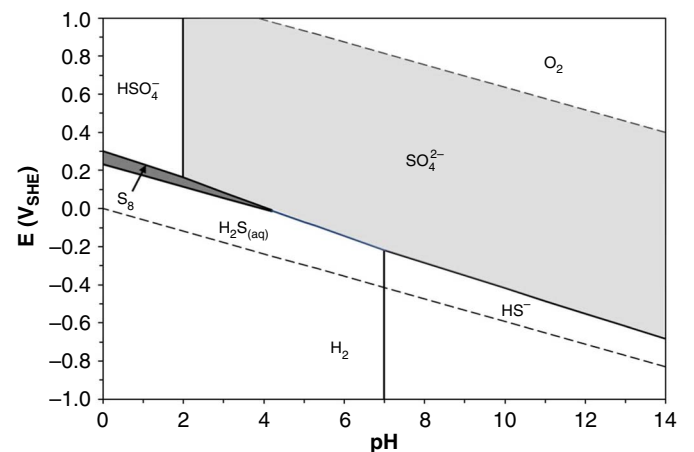
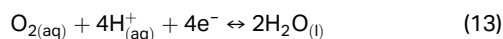
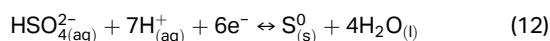
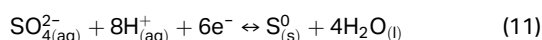
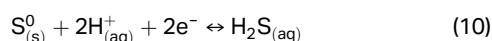
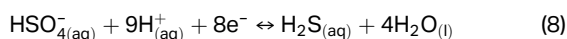
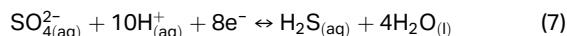


**FIGURE 2.** Pourbaix diagram of the H<sub>2</sub>S–H<sub>2</sub>O system (298.15 K, 1 atm, p<sub>H<sub>2</sub>S</sub> = 0.01 bar [1 v%]).

reactions shown here only involve the most thermodynamically stable species (e.g., only  $\text{SO}_4^{2-}$ , no  $\text{S}_2\text{O}_3^{2-}$ ). It should be noted that there is no oxygen in these reactions—here, the oxygen effect is reflected by the potential of the electrode, which is supposed to be pushed to the positive side due to the oxygen reduction reaction (Reaction [13]). It shows that at pH 5, the steel surface must be polarized to above 0  $V_{\text{SHE}}$  for  $\text{H}_2\text{S}$  to be oxidized. The measured OCP in the corrosion test was usually not as high as 0  $V_{\text{SHE}}$ . Assuming that the OCP can be used to represent the electrochemical potential of the system, the oxidation of dissolved  $\text{H}_2\text{S}$  should not happen. However, the diagram clearly identifies conditions when oxidation of  $\text{H}_2\text{S}$  into elemental sulfur and sulfates is thermodynamically possible.



A second Pourbaix diagram was developed considering a lower  $\text{H}_2\text{S}$  content (4 Pa [0.04 mbar], Figure 3) that corresponds to the baseline condition in the previous parametric studies (indicated with a small rectangle in the diagram). These conditions led to pitting corrosion. This diagram shows that the oxidation of dissolved  $\text{H}_2\text{S}$  was also not thermodynamically favored in these conditions. In addition, elemental sulfur is not predicted to be stable under any conditions, as opposed to what is shown with a higher  $\text{H}_2\text{S}$  content [1,000 Pa (0.01 bar), Figure 2]. In other words,  $\text{H}_2\text{S}$  can only be oxidized into  $\text{SO}_4^{2-}$  directly when the  $\text{H}_2\text{S}$  content is sufficiently low. Again, if the measured OCP

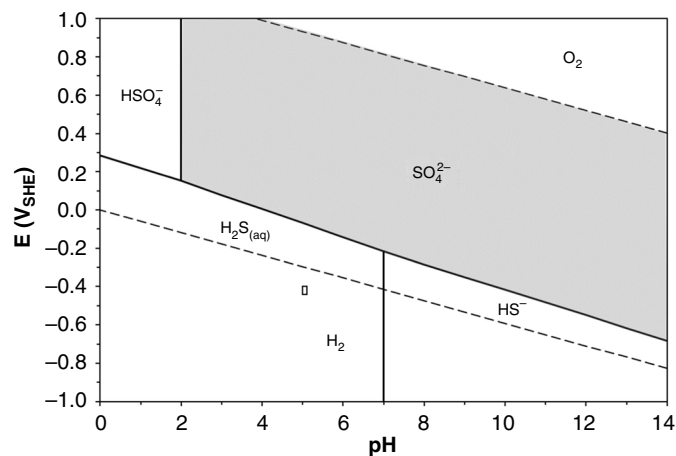
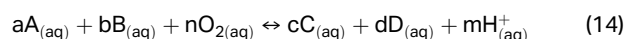


**FIGURE 3.** Pourbaix diagram of  $\text{H}_2\text{S}$ – $\text{H}_2\text{O}$  system (298.15 K, 1 atm,  $p\text{H}_2\text{S} = 0.04$  mbar [40 ppm]). The small rectangle ( $E = -440$  mV to  $-400$  mV,  $p\text{H}_{(\text{bulk})} = 5.00$  to 5.10) in the diagram is the baseline condition in terms of localized corrosion in marginally sour environments.

during the corrosion experiments is representative of the electrochemical potential of the system, there should be no oxidation of dissolved  $\text{H}_2\text{S}$ . However, as it will be shown later on, experimental observations seem to indicate otherwise, as a decrease in pH, which can be associated with  $\text{H}_2\text{S}$  oxidation, as well as direct measurement of  $\text{SO}_4^{2-}$  in the water samples, were observed during the test.

Figures 2 and 3 show that the electrode must be polarized into a more positive potential to enable the oxidation of dissolved  $\text{H}_2\text{S}$  in anoxic environments. However, the presence of some  $\text{O}_2$  is not reflected in the measured electrode potential indicated in Figure 3 (the latter reflecting the mixed potential of the corroding Fe surface rather than the bulk aqueous conditions). What is more relevant here than the corroding surface is how much oxygen is needed to enable the oxidation of dissolved  $\text{H}_2\text{S}$ . Therefore, the oxidation driving force in the diagram should be changed from potential (concentration of electrons) to concentration of dissolved oxygen in this system. The phase equilibrium diagram in Figure 4 was drawn to identify the threshold of dissolved oxygen concentration enabling  $\text{H}_2\text{S}$  oxidation. The thermodynamic data again comes from the literature.<sup>32</sup> The main idea is to correlate oxygen concentration with pH based on the Gibbs free energy. Therefore, this phase equilibrium diagram is a prediction tool similar to the Pourbaix diagram but now reflecting aqueous solution conditions. Several of the redox reactions considered are listed in Reactions (1) through (4); the rest are similar oxidation reactions with  $\text{HS}^-$  and  $\text{S}^{2-}$  rather than  $\text{H}_2\text{S}_{(\text{aq})}$ . The equilibrium constants associated with these reactions are calculated according to their associated standard Gibbs free energies. The reaction quotient can be written as shown in Equation (15), considering a generalized form of the redox reaction, shown in Reaction (14). Therefore, the equilibrium concentration of one reactant or product can be calculated from the equilibrium constant and concentrations of the remaining reactants and products (Equation [16]). Reactions that do not produce  $\text{H}^+$  are reflected as horizontal lines in the diagram. Similarly, reactions that do not involve  $\text{O}_2$  are reflected as vertical lines in the diagram.



$$K_c = \frac{[\text{C}]^c [\text{D}]^d [\text{H}^+]^m}{[\text{A}]^a [\text{B}]^b [\text{O}_{2(\text{aq})}]^n} \quad (15)$$

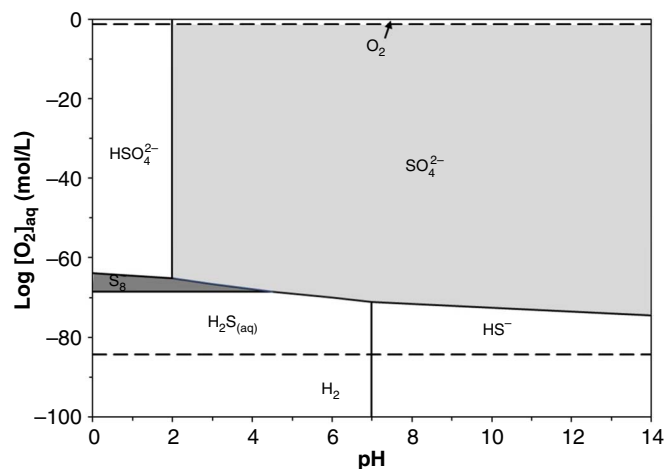


**FIGURE 4.** Phase equilibrium diagram of the  $\text{H}_2\text{S}$ – $\text{O}_2$ – $\text{H}_2\text{O}$  system (298.15 K, 1 atm,  $p\text{H}_2\text{S} = 0.01$  bar [1 v%]).

$$\log[O_{2(aq)}] = \frac{1}{n}(-mpH + c \log[C] + d \log[D] - \text{alg}[A] - b \log[B] - \log K_c) \quad (16)$$

Using the method described above, a phase equilibrium diagram plotting  $\log[O_{2(aq)}]$  vs. pH (Figure 4) was drawn for the  $H_2S-O_2-H_2O$  system at 298.15 K, 1 atm with 1 v%  $H_2S$ . The predictions in this work were compared with commercial software (Geochemist's WorkBench) and its database.<sup>35-36</sup> As a result, it showed good agreement. The diagram shows that when  $pH < 4.5$ , dissolved  $H_2S$  is predicted to be readily oxidized into elemental sulfur, then further oxidized into sulfate with higher  $O_2$  content. This reaction is thermodynamically predicted to occur even with  $O_{2(aq)}$  concentrations far below the  $ppt_{(w)}$  level. By comparison, the lowest residual dissolved oxygen concentration measured during all the experimental series was of the order of  $ppb_{(w)}$ ,<sup>7</sup> which should be more than enough to enable this conversion. This means that oxidation of dissolved  $H_2S$  is thermodynamically possible under the experimental conditions associated with sour corrosion studies. The extent and speed of this reaction are indeed not predicted by these equilibrium diagrams. The observations derived from the  $\log[O_{2(aq)}]$  vs. pH diagram are consistent with those from the E-pH diagram (Figure 2), in the sense that both diagrams identify conditions when  $H_2S$  can indeed be oxidized into elemental sulfur or sulfates.

To better simulate the experimental conditions corresponding to the marginally sour environments of this study, another  $\log[O_{2(aq)}]$  vs. pH phase equilibrium diagram (Figure 5) was drawn for the  $H_2S-O_2-H_2O$  system at 298.15 K, 1 atm with 4 Pa (40 ppm<sub>v</sub> in concentration)  $H_2S$ . The conditions corresponding to the baseline experiments are depicted as a small rectangle in the diagram. Some differences exist when compared with the equilibrium diagram developed for a higher concentration of  $H_2S$  (Figure 4). In the case of 40 ppm  $H_2S$ , dissolved  $H_2S$  can be oxidized into sulfate directly, and the zone of elemental sulfur stability does not exist. An important finding is that the dissolved  $H_2S$  can indeed be oxidized considering the baseline condition. This seems to be inconsistent with the E-pH diagram generated for the same condition (Figure 3). The explanation is related to the fact that the reactions

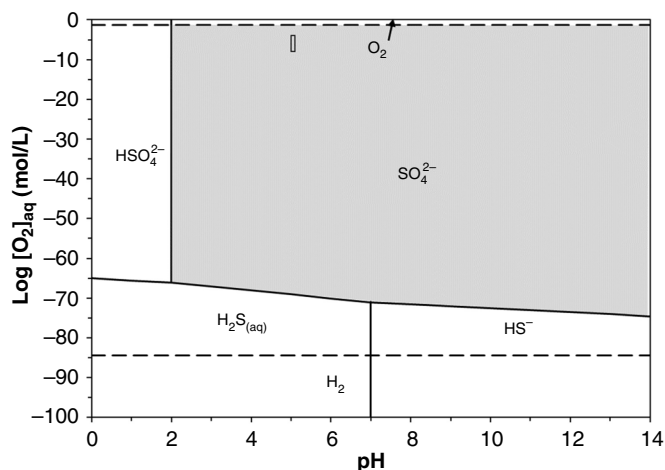


**FIGURE 5.** Phase equilibrium diagram of  $H_2S-O_2-H_2O$  system (298.15 K, 1 atm,  $p_{H_2S} = 0.04$  mbar [40 ppm<sub>v</sub>]). The small rectangle ( $[O_{2(aq)}] = 10^{-8}$  mol/L to  $10^{-4}$  mol/L,  $pH = 5.00$  to  $5.10$ ) in the diagram is the baseline condition in terms of localized corrosion in marginally sour environments.

between dissolved oxygen and dissolved  $H_2S$  did not occur at the surface of the working electrode. Therefore, the OCP may not be an accurate reflection of the electrochemical potential of the system, especially considering reactions occurring in the bulk solution. In other words, this finding suggests that while Pourbaix diagrams can effectively predict the thermodynamics of electrochemical and chemical reactions occurring on the substrate surface, other phase equilibrium diagrams may also be useful to characterize homogeneous reactions happening in the bulk solution and identify thermodynamically stable bulk species.

NACE standard TM 0177<sup>37</sup> states that "oxygen contamination is evident by a cloudy (opaque) appearance of the test solution," which corresponds to the formation of elemental sulfur. Because in marginally sour conditions elemental sulfur is not expected as a by-product of  $H_2S$  oxidation, the solution should remain transparent and clear even though sulfate species may be formed in the solution. Because whether an  $H_2S$  containing solution would turn to opaque when exposed to air depends on such conditions as temperature, pH, and  $H_2S$  concentration (or partial pressure in the corresponding gas phase), a third-phase equilibrium diagram (Figure 6) was developed to characterize this phenomenon based on various  $H_2S$  partial pressures ( $p_{H_2S} = 100,000$  Pa [1 bar], 10,000 Pa [0.1 bar], 1,000 Pa [0.01 bar], 100 Pa [1 mbar], 50 Pa [0.5 mbar], and 30 Pa [0.3 mbar]) at 25°C. According to this diagram, elemental sulfur formation, for example, is expected when  $p_{H_2S} > 1,000$  Pa (0.01 bar) at pH 5 and when  $p_{H_2S} > 30$  Pa (300 ppm<sub>v</sub> in concentration) at pH 1.

Other less stable oxidation products of dissolved  $H_2S$ , such as  $SO_3^{2-}$  and  $S_2O_3^{2-}$ , can be included in the phase equilibrium diagram if the presence of the most stable species ( $SO_4^{2-}$  for example) is suppressed.<sup>32</sup> Although they are not as stable thermodynamically speaking, they could still be detected experimentally by analyzing the composition of the aqueous phase if their formations are kinetically favored.<sup>19-20</sup> In summary, the oxidation of  $H_2S$  should generate  $SO_4^{2-}$  although traces of  $SO_3^{2-}$  and  $S_2O_3^{2-}$  could also be detected—elemental sulfur would only precipitate if the  $H_2S$  content is significantly higher. In marginally sour environments, considering the low content of  $H_2S$ ,  $SO_4^{2-}$  is probably the most prominent detectable product, although equilibrium diagrams are not indicators of reaction kinetics.

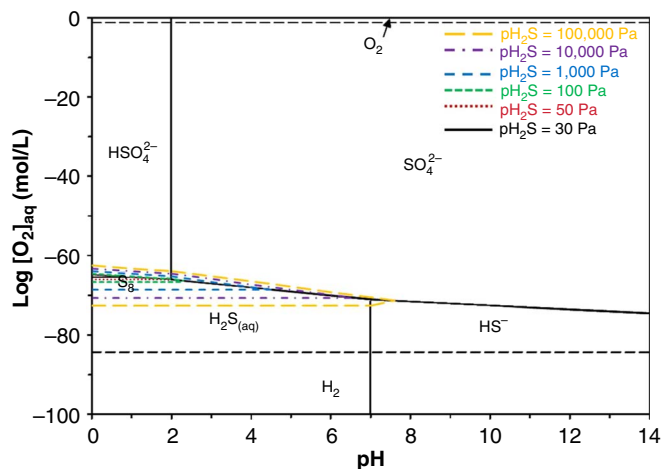
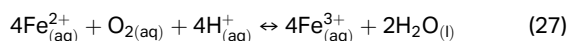
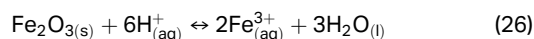
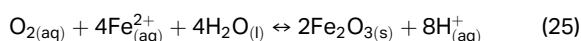
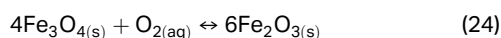
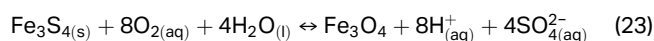
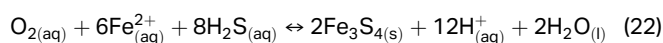
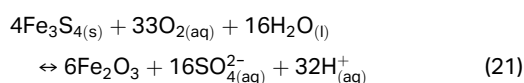
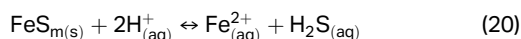
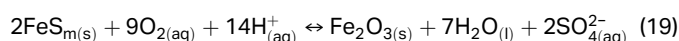
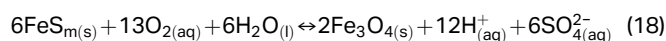
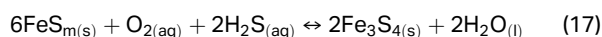


**FIGURE 6.** Using phase equilibrium diagram of  $H_2S-O_2-H_2O$  system to predict formation of elemental sulfur (298.15 K, 1 atm).

## THERMODYNAMICS OF THE OXIDATION OF MACKINAWITE CORROSION PRODUCT LAYER

The prediction exercise as described above was repeated considering the mackinawite—O<sub>2</sub>—H<sub>2</sub>O system to investigate the overall effect of oxygen on the corrosion product layers in the marginally sour environments, using Reactions (17) through (27). These reactions revealed that the most stable sulfur-containing product during the transition from iron sulfides to iron oxides is SO<sub>4</sub><sup>2-</sup>, not elemental sulfur. Therefore, it makes sense that no elemental sulfur was observed in the acquired *in situ* Raman spectrum for the partially oxidized mackinawite.<sup>5</sup>



In the absence of oxygen, the chemisorption of H<sub>2</sub>S and precipitation of the thin mackinawite layer on the steel surface can be illustrated by a Pourbaix diagram.<sup>5</sup> In this work, the effect of the presence of dissolved oxygen is presented as a log[O<sub>2(aq)</sub>] vs. pH phase equilibrium diagram, as shown in Figure 7 that considers 0.01 bar H<sub>2</sub>S. This diagram indicates that mackinawite can be oxidized into greigite, magnetite or hematite depending on the pH.

Figure 8, which depicts a marginally sour environment with 4 Pa (40 ppm<sub>v</sub>) in concentration of H<sub>2</sub>S, shows that mackinawite can only be oxidized to magnetite and hematite when pH > 6. The specific conditions of the baseline test (bulk pH 5 and 20 ppb<sub>w</sub>) of dissolved oxygen are indicated in Figure 8 by the small rectangle. It clearly shows that hematite is the most stable species in these conditions. The chemisorbed or precipitated FeS layer formed during the experiments would

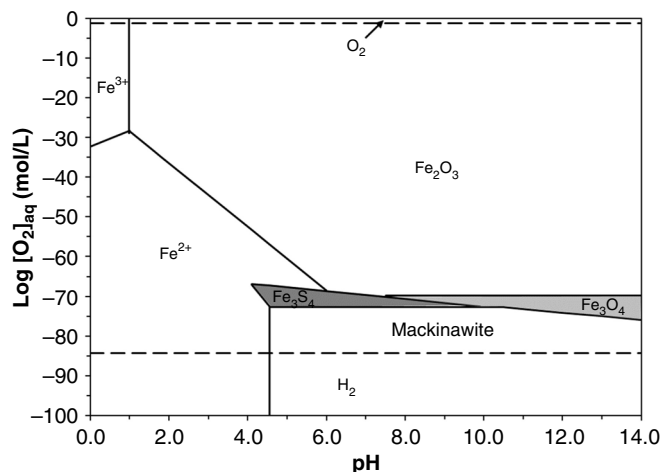


FIGURE 7. Phase equilibrium diagram of the mackinawite—O<sub>2</sub>—H<sub>2</sub>O system (298.15 K, 1 atm, pH<sub>2</sub>S = 0.01 bar [1 v%]).

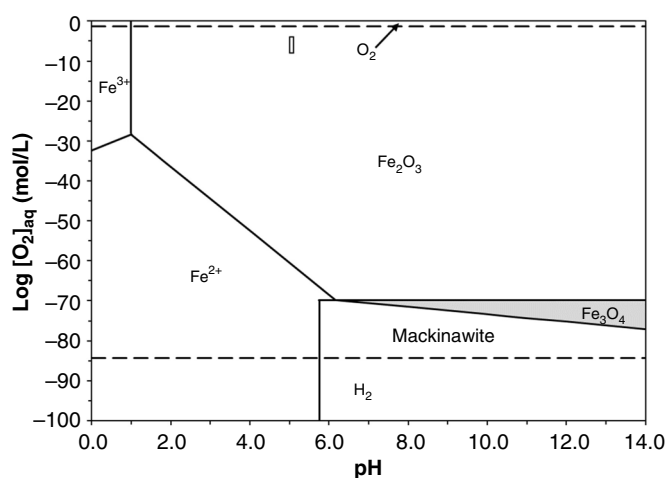


FIGURE 8. Phase equilibrium diagram of Mackinawite—O<sub>2</sub>—H<sub>2</sub>O system (298.15 K, 1 atm, pH<sub>2</sub>S = 0.04 mbar [40 ppm<sub>v</sub>]). The small rectangle ([O<sub>2(aq)</sub>] = 10<sup>-8</sup> mol/L to 10<sup>-4</sup> mol/L, pH = 5.00 to 5.10) in the diagram is the baseline condition in terms of localized corrosion in marginally sour environments.

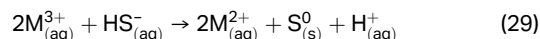
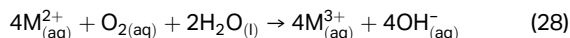
gradually dissolve, releasing Fe<sup>2+</sup>, which ends up being oxidized into hematite. These reactions would also generate sulfates as by-products. These statements, of course, do not take into account the kinetics of the reactions. Based on the previous experimental observations at various oxygen concentrations, hematite was seldomly detected via *in situ* analysis. Instead, when [O<sub>2(aq)</sub>] is between 20 ppb<sub>w</sub>) and 40 ppb<sub>w</sub>), only magnetite (not hematite) was detected on the corroding steel surface using *in situ* Raman spectroscopy.<sup>5</sup> However, *ex situ* Raman microscopy did reveal the presence of hematite after exposure of the precipitated layer to air plus laser-induced heating.<sup>5</sup>

In summary, the thermodynamic predictions and the experimental observations suggest that the chemisorbed or precipitated FeS layer can be oxidized in the presence of dissolved oxygen into iron oxides (magnetite being more kinetically favored over hematite in the presence of traces of oxygen). This scenario is postulated to describe how the observed pitting initiated on X65 steel during experiments conducted in marginally sour environments.<sup>5</sup>

## KINETICS OF THE OXIDATION OF DISSOLVED H<sub>2</sub>S AT LOW TEMPERATURES

### 5.1 | Background and Previous Results

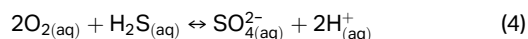
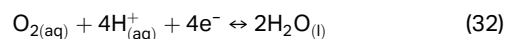
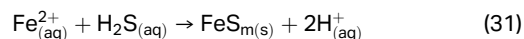
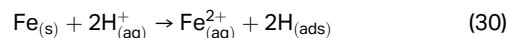
Kinetically, oxidation of gaseous H<sub>2</sub>S cannot readily happen without a catalyst and high temperature.<sup>32</sup> However, H<sub>2</sub>S oxidation can occur in an aqueous solution near room temperature;<sup>19-20,31</sup> the proposed mechanism involving a catalytic cycle and transition metals.<sup>25</sup> Transition metal ions such as Fe<sup>2+</sup>, Mn<sup>2+</sup>, Ni<sup>2+</sup>, and Co<sup>2+</sup> could serve as a catalyst, as shown in Reactions (28) and (29) where M therein is representative of any of the aforementioned transition metals.<sup>38</sup> The catalyst has no selectivity in terms of eventual products (S<sup>0</sup> or SO<sub>4</sub><sup>2-</sup>).<sup>24</sup>



The API 5L X65 steel used in this study contains mainly Fe (97.32 wt%), a significant amount of Mn (1.51 wt%), and traces of Ni (0.29 wt%) and Cu (0.17 wt%).<sup>3</sup> As proven in other kinetics-related research,<sup>33</sup> at pH 6.8, with 0.005 mg/L of Ni<sup>2+</sup>, 200 mg/L H<sub>2</sub>S<sub>(aq)</sub> could bring the O<sub>2(aq)</sub> down from 7 mg/L to 3 mg/L within 240 s. The same research also found that at pH 6.5, with 5 mg/L of Fe<sup>2+</sup>, 200 mg/L H<sub>2</sub>S could bring the O<sub>2(aq)</sub> down from 6 mg/L to 2 mg/L within 1,000 s.<sup>24</sup> Considering the baseline condition in marginally sour corrosion [X65 in 40 ppm<sub>(v)</sub> (= 0.13 mg/L) H<sub>2</sub>S at 30°C, pH 5.01±0.01], the measured [Fe<sup>2+</sup>] was usually around 20 mg/L after 7 d of exposure. Therefore, [Ni<sup>2+</sup>] dissolving proportionally should be up to 0.06 mg/L. The measured Fe<sup>2+</sup> and Ni<sup>2+</sup> concentrations in the marginally sour environments are within the same order of magnitude as has been reported in the literature above on catalysis and should be enough to catalyze the oxidation of H<sub>2</sub>S<sub>(aq)</sub> by O<sub>2(aq)</sub>.

As shown in the part II paper of this research project,<sup>7</sup> pH increases gradually when [O<sub>2</sub>]<sub>(aq)</sub> > 20 ppb<sub>(w)</sub>; pH decreases gradually when [O<sub>2</sub>]<sub>(aq)</sub> < 3 ppb<sub>(w)</sub>; and pH fluctuates around 5.01 when 3 ppb<sub>(w)</sub> < [O<sub>2</sub>]<sub>(aq)</sub> < 20 ppb<sub>(w)</sub>. This indicates that there are multiple reactions affecting pH at the same time in the system. Some of these reactions are well known: electrochemical dissolution of metal consumes H<sup>+</sup> via the reduction reaction (Reaction [30]); precipitation of FeS produces H<sup>+</sup> (Reaction [32]); reduction of O<sub>2</sub> consumes H<sup>+</sup> (Reaction [32]); and oxidation of H<sub>2</sub>S produces H<sup>+</sup> (Reaction [4]). For every 1 mol of O<sub>2</sub> that is reduced, 4 mol of H<sup>+</sup> is consumed. Therefore, when the oxygen content is higher, its effect on increasing the pH would be relatively more pronounced. However, the concentration of O<sub>2(aq)</sub> in solution is so low that the contribution of the reduction of O<sub>2(aq)</sub> on pH change may not be significant. The iron dissolution reactions and the precipitation of FeS could have counteracting effects. However, because not all of the dissolved Fe is expected to precipitate as FeS, the overall effect should lead to an increase in pH. As for the oxidation of H<sub>2</sub>S, its contribution to pH change is difficult to evaluate, especially because the kinetics are dependent on the catalyst. It is unclear which of the two reactions, dissolved oxygen reduction or H<sub>2</sub>S oxidation, will have the stronger effect on pH, although it can be speculated that the likelihood of a dissolved oxygen molecule being reduced at the metal surface is higher than two molecules of dissolved oxygen and H<sub>2</sub>S reacting at a catalyst site. When the corrosion rate was high, the pH increased because of the effect of the corrosion reaction that dominates

the other two reactions, although the dissolved oxygen content was paradoxically higher. When the corrosion rate was lower, which corresponded to a lower dissolved oxygen content, the pH decreased due to the oxidation of H<sub>2</sub>S<sub>(aq)</sub>—in this case the reduction of O<sub>2(aq)</sub> was negligible.



Separation of sulfide, sulfite, sulfate, thiosulfate, and polysulfide through HPLC remains an analytical challenge.<sup>39-40</sup> Fortunately, according to the thermodynamic predictions in the *Thermodynamics of The Oxidation of Dissolved H<sub>2</sub>S at Low Temperatures* section of this paper, sulfate is the most stable and most common oxidation product of H<sub>2</sub>S. Therefore, a simple and effective analytical method for water samples in marginally sour environments was used to verify the predictions by the phase equilibrium diagram here. The [SO<sub>4</sub><sup>2-</sup>] was measured by the SulfaVer 4<sup>†</sup> method<sup>®</sup> (using BaCl<sub>2</sub>) using ultraviolet (UV)/Vis spectroscopy to verify if catalytic oxidation was happening in this system. At the same time, the pH was left uncontrolled during the entire 7 d experiment to observe how much the pH would drop.

### 5.2 | Experimental Procedure

As depicted in Figure 9, a 2 L glass cell reactor with a specially designed stainless lid featuring five polyether ether ketone (PEEK) sampling ports (one for an epoxy-sealed X65 working electrode, four for half-square inch X65 steel corrosion coupons) was used in the experiments. pH was monitored but

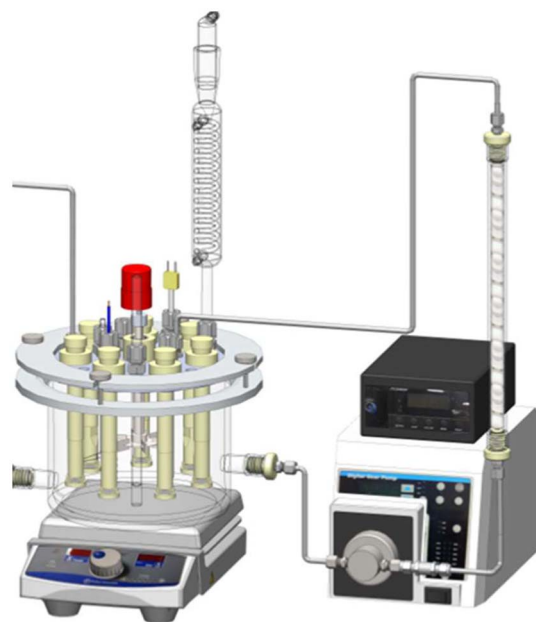


**FIGURE 9.** Stable solution chemistry system for a small-scale lab test with fixed specimen holders and rotating impeller in a glass cell (images courtesy of Cody Shafer, ICMT).

<sup>†</sup> Trade name.

not controlled in these experiments. The testing condition was at 30°C, 1 bar total pressure. The beginning pH = 5.01±0.01. The stir bar rotation speed was 300 rpm. A 1 wt% NaCl solution was prepared. CO<sub>2</sub> gas was used to sparge the sealed system for at least 2 h to bring the dissolved oxygen concentration to less than 10 ppb<sub>(w)</sub>, then a mixture of 100 ppm<sub>(v)</sub> H<sub>2</sub>S in CO<sub>2</sub> was sparged into the sealed system. Gas flows were adjusted to control the ratio between the pure CO<sub>2</sub> and H<sub>2</sub>S/CO<sub>2</sub> mixed gas flow to achieve the 4 Pa (40 ppm<sub>(v)</sub> in concentration) of H<sub>2</sub>S, which was verified by a GASTEC<sup>†</sup> pump and glass detector tube from a testing port on the gas route. The H<sub>2</sub>S and CO<sub>2</sub> gases used contains a measured [O<sub>2</sub>]<sub>(aq)</sub> less than 0.6 ppb<sub>(w)</sub>. The [O<sub>2</sub>]<sub>(aq)</sub> in the glass cell during experiments was controlled by cleaning and tightening of all the contact surfaces. Therefore, each experiment achieved [O<sub>2</sub>]<sub>(aq)</sub> as monitored by a HACH<sup>®</sup> Orbisphere 410<sup>†</sup> Controller O<sub>2</sub> and a M1100<sup>†</sup> Oxygen Sensor connected at the outlet of the gas hose of a glass cell before scrubber. The electrolyte was sparged with the H<sub>2</sub>S/CO<sub>2</sub> mixture for 5 h prior to specimen loading. A water sample was taken after the 5 h of sparging. Then the X65 specimens were loaded into the system after this measurement. The corrosion experiment was started with the pH monitored and recorded during the entire experimental process. Water samples were again retrieved after 5 d and 7 d of the corrosion experiment and analyzed with the HACH<sup>®</sup> DR6000<sup>†</sup>™ UV/Vis spectrophotometer to detect if there was any SO<sub>4</sub><sup>2-</sup>. A BaCl<sub>2</sub> reagent was used. A standard calibration curve was made. The testing limit is 2 mg/L. The 2 L aqueous solution was extracted with toluene at 50°C after the corrosion experiment to determine if any elemental sulfur was present. The extracted concentrated toluene solution was placed into a glass petri dish for Raman microscopy analysis.

### 5.3 | Results and Discussion

The experimental results are shown in Figure 10. Overall, the average [O<sub>2</sub>]<sub>(aq)</sub> was measured to be ca. 7 ppb<sub>(w)</sub>. The spikes were caused by opening the system to load or retract the coupons. As shown in the timeline of the experimental

procedures, a water sample was taken after 5 h of sparging before the steel specimens were loaded. At that point, the measured [SO<sub>4</sub><sup>2-</sup>] was zero. When the specimens were loaded, a sharp increase of [O<sub>2</sub>]<sub>(aq)</sub> was measured, but the [O<sub>2</sub>]<sub>(aq)</sub> content decreased quickly and reached a stable level of around 7 ppb<sub>(w)</sub> in the liquid phase. After 5 d, the measured [SO<sub>4</sub><sup>2-</sup>] was 3 mg/L; after 7 d, it was 4 mg/L. This reading is indeed small but has to be compared with the concentration of O<sub>2</sub> in this system. Actually, the [SO<sub>4</sub><sup>2-</sup>] measurements in the related research<sup>19-20</sup> also only found small concentrations. The trend of pH changes agreed with the production of SO<sub>4</sub><sup>2-</sup> in that it began to drop after the steel specimens were inserted in the solution. An estimation of the generated concentration of [SO<sub>4</sub><sup>2-</sup>] corresponding to a pH drop from 5.0 to 4.6 in 24 h via oxidation Reaction (4) yielded values around 5 mg/L [SO<sub>4</sub><sup>2-</sup>] and consumption of 0.6 ppb<sub>(w)</sub>/min of O<sub>2</sub>. A more precise calculation should include the effect of the O<sub>2</sub> diffusion and reduction, as well as the consumption of H<sub>2</sub>S through the corrosion reactions and FeS precipitation. In summary, the simultaneous increase in H<sup>+</sup> and SO<sub>4</sub><sup>2-</sup> concentrations seems to prove that the catalytic oxidation of H<sub>2</sub>S occurred at the low dissolved oxygen concentration present. Coincidentally, this effect is only visible when the oxygen content is low enough to ensure that the FeS layer remains undamaged (i.e., the corrosion rate remains low). It should also occur at higher oxygen content, but its effect on bulk pH would be masked by the products of the corrosion reactions. It is postulated that this reaction can also play a role in the pitting process, contributing to the local acidification of the pit.

Another point worth discussing is the accuracy of this measurement. The measurement range of the SulfaVer 4 method<sup>®</sup> (BaCl<sub>2</sub>) by UV/Vis is 2 mg/L to 70 mg/L. Therefore, readings of 3 mg/L and 4 mg/L may quantitatively not be very convincing because they are very near the detection limit. However, the accuracy of the measurement is not as important as the knowledge that the reaction (H<sub>2</sub>S oxidation) does occur. The measurement method is based on the reaction between Ba<sup>2+</sup> and SO<sub>4</sub><sup>2-</sup> to form a homogeneous white solid suspension of

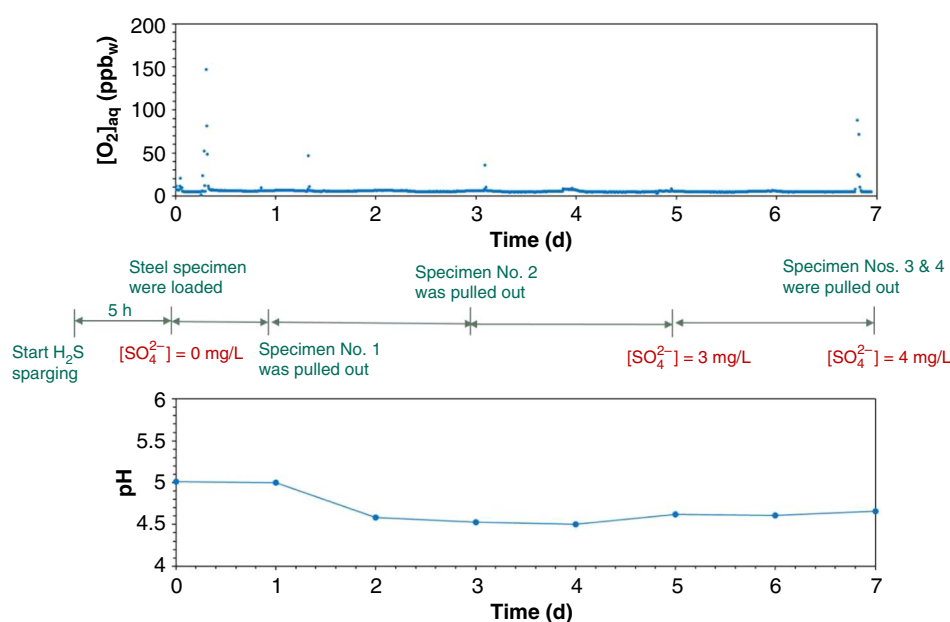


**FIGURE 10.** Water chemistry analysis by UV/Vis and pH monitoring (30°C, initial pH = 5.01, pCO<sub>2</sub> = 0.97 bar, pH<sub>2</sub>S = 40 mbar, and [O<sub>2</sub>]<sub>(aq)</sub> = 7 ppb<sub>(w)</sub>).

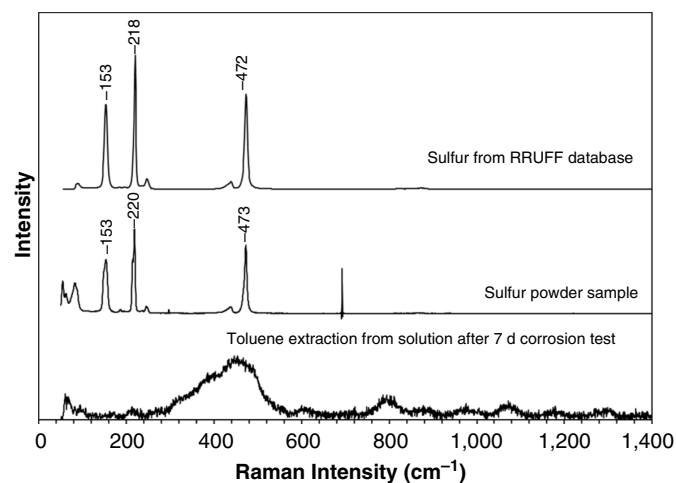


**FIGURE 11.** Toluene extraction after 7 d experiment for Raman analysis detection of elemental sulfur.

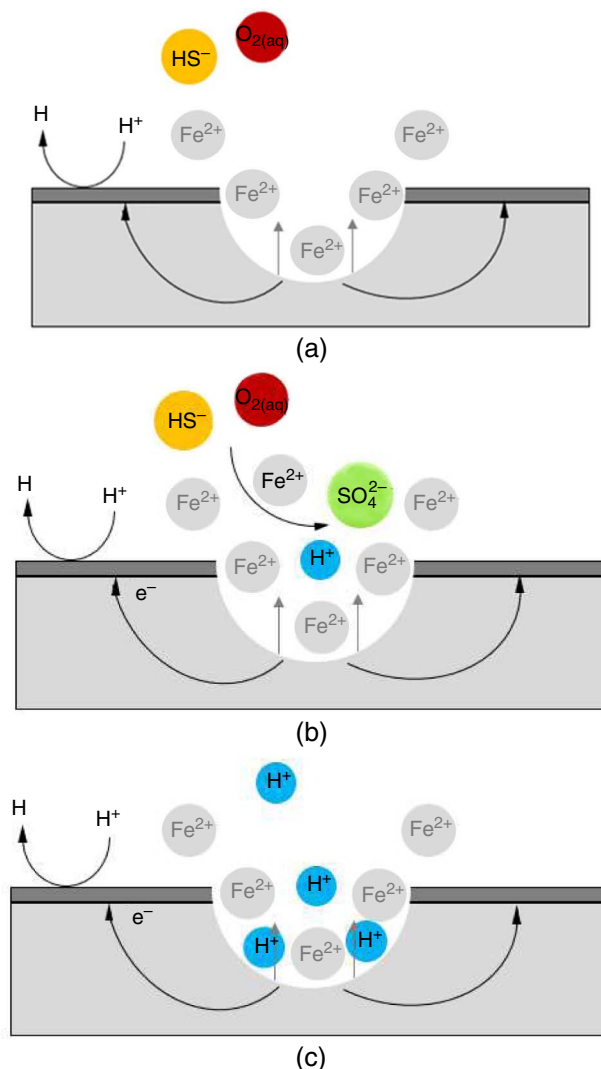
BaSO<sub>4</sub> (Reaction [33]). Naked eye observation of the solution during the measurement clearly showed that the reaction was indeed happening giving confidence in the overall findings.



Figure 11 shows Raman results from toluene extraction of the 2 L solution after a 7 d corrosion experiment in comparison to the standard RRUFF database<sup>41</sup> (top) and a commercial sulfur powder measured with the same equipment in the author's lab (middle). The peaks at 153 cm<sup>-1</sup>, 218 cm<sup>-1</sup>, and 472 cm<sup>-1</sup> of Raman spectra are uniquely characteristic of elemental sulfur. The results (the bottom curve) did not capture the fingerprint peaks of elemental sulfur compared with the sulfur powder sample or the RRUFF database value. This observation verified the findings in the previous thermodynamic prediction that no elemental sulfur was generated in this system (Reactions [18] and [19]).

### PIT PROPAGATION MECHANISM: SOLUTION ACIDIFICATION NEAR STEEL SURFACE BY CATALYTIC OXIDATION OF H<sub>2</sub>S<sub>(AQ)</sub>

The previous sections helped identify possible reactions that could explain the in situ formation of oxides and the acidification of the solution in marginally sour corrosion with traces of oxygen. A qualitative pit propagation mechanism is proposed here considering: (1) galvanic coupling between the small actively corroding anode (exposed to a solution containing H<sub>2</sub>CO<sub>3</sub>) and the larger protected surface covered by FeS acting as the cathode and (2) the pit acidification caused by catalytic oxidation of H<sub>2</sub>S<sub>(aq)</sub> by O<sub>2(aq)</sub>. Based on the pH monitoring observation in this work, the pit acidification, in this case, is very mild (from 5.0 to 4.5). It is not comparable to the large pH shifts expected for the passive system, well-known pit acidification theory. Therefore, the implication of this mild pit acidification in marginally sour environments is mostly related to a decrease in FeS saturation value inside the pit, which prevents the regeneration of a protective FeS layer despite a high [Fe<sup>2+</sup>] in the pit. The pit acidification is not thought to drive the increase in corrosion rate, at least at the same level as the galvanic coupling does. This process is represented in Figure 12. In this scenario, due to the conductivity of mackinawite



**FIGURE 12.** Proposed pit propagation mechanism (a) [Fe<sup>2+</sup>] is higher inside the pit, (b) Catalytic oxidation of H<sub>2</sub>S<sub>(aq)</sub> by O<sub>2(aq)</sub>, most significant where [Fe<sup>2+</sup>] is elevated, and (c) [H<sup>+</sup>] is higher inside the pit.

and the geometry of the small anode area inside the pit, the current density inside the pit is much larger than at the outside cathode area. At the same time, H<sub>2</sub>S<sub>(aq)</sub> is oxidized by dissolved O<sub>2</sub>, even at low temperatures. The reaction is catalyzed by Fe<sup>2+</sup>, which is most abundant inside the pit. This reaction releases H<sup>+</sup> and SO<sub>4</sub><sup>2-</sup> as products. Therefore, inside the pit a pH result is lower than in the bulk solution. These factors taken together constitute a credible pit propagation mechanism in marginally sour environments. There was warning long ago that oxygen ingress in sour corrosion could acidify the solution or precipitate elemental sulfur,<sup>42</sup> and even cause pitting.<sup>19</sup> However, these observations were not investigated systematically until this work.

### CONCLUSIONS

> In marginally sour environments with traces of oxygen ingress where pitting was observed repeatedly, the modeled potentiodynamic sweep showed that the contribution of the O<sub>2</sub> reduction to the overall cathodic reaction was not prominent enough to provoke a significant increase of corrosion rate observed with increased but limited ingress of oxygen.

- Thermodynamic calculation predicted that an extremely low concentration of oxygen (i.e., at the ppb<sub>(w)</sub> level) would be enough to oxidize dissolved H<sub>2</sub>S at low temperatures, be it in the presence of catalysts such as Fe<sup>2+</sup> or Ni<sup>2+</sup>. Measurements proved that H<sup>+</sup> and SO<sub>4</sub><sup>2-</sup>, the products of H<sub>2</sub>S oxidation, were formed during the corrosion experiments with traces of oxygen.
- The thermodynamic calculation also predicted that the mackinawite corrosion product layer could be oxidized into magnetite and finally hematite in the presence of traces of oxygen in the aqueous solution.
- Both the thermodynamic calculations and the experimental observations presented in this work revealed that the pitting mechanism of mild steel in marginally sour environments was not related to a partially formed layer, but rather to a layer that was partially damaged by reaction with dissolved oxygen.
- Consistent with the experimental observations, pit acidification and galvanic coupling were proposed as the cause of pit propagation in this study.

## ACKNOWLEDGMENTS

This work was supported by the corrosion center joint industry project; Institute for Corrosion and Multiphase Technology, Ohio University, 342 West State Street, Athens, OH, 45701, USA.

## References

1. S. Navabzadeh Esmaeely, W. Zhang, B. Brown, M. Singer, S. Nešić, *Corrosion* 73, 9 (2017): p. 1098-1106.
2. W. Zhang, "Initiation and Propagation of Localized Corrosion of Mild Steel in Marginally Sour Environments" (Ph.D. diss., Dept. Chem. & Biomol. Chem. Eng., Ohio University, Athens, 2020), p. 48.
3. W. Zhang, B. Brown, D. Young, Gheorghe Bota, S. Nešić, M. Singer, *Corros. Sci.* 183 (2021): article id 109305.
4. N. Yaakob, "Top of the Line Corrosion in CO<sub>2</sub>/H<sub>2</sub>S Environments" (Ph.D. diss., Dept. Chem. & Biomol. Chem. Eng., Ohio University, Athens, 2014).
5. W. Zhang, D. Young, B. Brown, M. Singer, *Corros. Sci.* 184 (2021): article id 109337.
6. H. Uhlig, *Corros. Sci.* 19 (1979): p. 777-791.
7. G.S. Frankel, *J. Electrochem. Soc.* 145, 6 (1998): p. 2186-2198.
8. S.T. Pride, J.R. Scully, J.L. Hudson, *J. Electrochem. Soc.* 141, 11 (1994): article id 3028.
9. J.R. Galvele, *J. Electrochem. Soc.* 123 (1976): p. 464-474.
10. M. Scholz, "Coagulation and Flocculation," in *Wetland Systems to Control Urban Runoff* (Amsterdam, Netherlands: Elsevier B.V., 2006), p. 37-46.
11. H. Strehlow, "Mechanisms of Pitting Corrosion," in *Corrosion Mechanisms in Theory and Practice*, ed. P. Marcus (New York, NY: Marcel Dekker, Inc., 2002), p. 217-242.
12. J. Han, S. Nešić, Y. Yang, B.N. Brown, *Electrochim. Acta* 56 (2011): p. 5396-5404.
13. J. Han, "Galvanic Mechanism of Localized Corrosion for Mild Steel in Carbon Dioxide Environments" (Ph.D. diss., Dept. Chem. & Biomol. Chem. Eng., Ohio University, Athens, 2009).
14. H. Li, "A Mechanistic Model for CO<sub>2</sub> Localized Corrosion of Carbon Steel" (Ph.D. diss., Dept. Chem. & Biomol. Chem. Eng., Ohio University, Athens, 2011).
15. M. Singer, "Part VI: Advancements in Modeling and Prediction Top-of-the-Line Corrosion," in *Trends in Oil and Gas Corrosion Research and Technologies*, 1st ed., ed. A.M. El-Sherik (Cambridge, United Kingdom: Woodhead Publishing, 2017), p. 698-699.
16. J. Ning, Y. Zheng, B. Brown, D. Young, S. Nešić, *Corrosion* 73 (2017): p. 155-168.
17. S. Navabzadeh, G. Bota, B. Brown, S. Nešić, *Corrosion* 74 (2018): p. 37-49.
18. C.I. Pearce, R.A.D. Patrick, D.J. Vaughan, *Rev. Mineral. Geochem.* 61 (2006): p. 127-180.
19. Y. Song, A. Palencsár, G. Svenningsen, J. Kvarekvål, T. Hemmingsen, "Effect of O<sub>2</sub> and Temperature on Sour Corrosion," *CORROSION* 2014, paper no. 4299 (Houston, TX: NACE, 2014).
20. M.D. Deffo Ayagou, C. Mendibide, C. Duret-Thual, J. Kittel, K. Belkhadiri, T.T. Mai Tran, E. Sutter, B. Tribollet, N. Ferrando, *Corrosion* 74, 11 (2018): p. 1192-1202.
21. K.Y. Chen, J. Carrell Morris, *Environ. Sci. Technol.* 6, 6 (1972): p. 529-537.
22. O.N. Kovalenko, N.N. Kundo, P.N. Kalinkin, *React. Kinet. Catal. Lett.* 72, 1 (2001): p. 139-145.
23. E.S. Snavely, F.E. Blount, "Rates of Reaction of Dissolved Oxygen with Scavengers in Sweet and Sour Brines," *CORROSION* 1969, paper no. 45 (Houston, TX: NACE, 1969).
24. A.K. Dalai, A. Majumdar, E.L. Tollefson, *Environ. Sci. Technol.* 33 (1999): p. 2241-2246.
25. D. Rickard, G.W. Luther III, *Chem. Rev.* 107 (2007): p. 514-562.
26. A. Anderko, P.J. Shuler, *Comput. Geosci.* 23, 6 (1997): p. 647-658.
27. L.G. Benning, R.T. Wilkin, H.L. Barnes, *Chem. Geol.* 167 (2000): p. 25-51.
28. Overview of FREECORP, Institute for Corrosion and Multiphase Technology, <http://www.icmt.ohio.edu/software/freecorp/help-overview.asp> (Dec. 28, 2020).
29. R.W. Revie, H.H. Uhlig, "Thermodynamics: Pourbaix Diagrams," in *Corrosion and Corrosion Control: An Introduction to Corrosion Science and Engineering*, 4th ed. (Hoboken, NJ: John Wiley & Sons, Inc., 2008), p. 43-46.
30. P. Kissinger, W.R. Heineman, *Laboratory Techniques in Electro-analytical Chemistry*, 2nd ed. (New York, NY: Marcel Dekker, Inc., 1996), p. 484-488.
31. J. Wang, *Analytical Electrochemistry*, 3rd ed. (Hoboken, NJ: John Wiley & Sons, Inc., 2006), p. 19-22.
32. G.H. Kelsall, I. Thompson, *J. Appl. Electrochem.* 23 (1993): p. 279-286.
33. L.V. Gurvich, I.V. Veyts, C.B. Alcock, eds., *Thermodynamic Properties of Individual Substances*, 4th ed. (New York, NY: Hemisphere Publishing Corp., 1989). Retrieved from "Thermodynamic Properties as a Function of Temperature, Section 5: Thermochemistry, Electrochemistry, and Kinetics," in *CRC Handbook of Chemistry and Physics*: 5-61~84.
34. M.W. Chase Jr., C.A. Davies, J.R. Downey Jr., D.J. Frurip, R.A. McDonald, A.N. Syverud, *J. Phys. Chem. Ref. Data* 14, Suppl. 1 (1985). Retrieved from "Thermodynamic Properties as a Function of Temperature, Section 5: Thermochemistry, Electrochemistry, and Kinetics," in *CRC Handbook of Chemistry and Physics*: 5-61~84.
35. The LLNL thermo database: thermo.tdat. This is the default dataset of thermodynamic data for the GWB applications. <https://www.gwb.com/thermo.php>.
36. The thermodynamic dataset from the U.S. Geological Survey's PhreeQC program with free access without any permission required within the U.S., formatted for the GWB applications: thermo\_phreeqc.tdat. <https://www.usgs.gov/software/phreeqc-version-3/>.
37. TM0177-2016-SG, "Laboratory Testing of Metals for Resistance to Sulfide Stress Cracking and Stress Corrosion Cracking in H<sub>2</sub>S Environments" (Houston, TX: NACE, 2016).
38. S. Ma, A. Noble, D. Butcher, R.E. Trouwborst, G.W. Luther III, *Estuarine, Coastal Shelf Sci.* 70 (2006): p. 461-472.
39. J. Rethmeier, A. Rabenstein, M. Langer, U. Fischer, *J. Chromatogr. A* 760 (1997): p. 295-302.
40. Y. Miura, Y. Matsushita, P.R. Haddad, *J. Chromatogr. A* 1085 (2005): p. 47-53.
41. RRUFF ID: R040135, University of Arizona Mineral Museum 5818, Locality: Sicily, Italy.
42. J.L. Crolet, M. Pourbaix, A. Pourbaix, "The Role of Trace Amounts of Oxygen on the Corrosivity of H<sub>2</sub>S Media," *CORROSION* 1991, paper no. 22 (Houston, TX: NACE, 1991).